



Cite this: DOI: 10.1039/c8sm02494d

Influence of Bénard–Marangoni instability on the morphology of drying colloidal films

Benjamin Sobac,^a Pierre Colinet^a and Ludovic Pauchard^b

The drying of colloidal suspensions is a very complex process leading to a sol–gel transition induced by solvent evaporation. The resulting film can even crack and delaminate. In this study, we investigate the drying process of a colloidal suspension with a highly volatile solvent and we show for initially millimeter-thick layers that the resulting pattern of delaminated plates considerably differs from what is usually observed for aqueous colloidal suspensions. Visualization using an IR camera reveals that hexagonal convection cells can develop during the drying of suspensions with a highly volatile solvent and may persist until the film consolidation. This leads to the formation of non-homogeneous films presenting surface corrugations. Thus, we highlight the importance of the hydrodynamics during the first phase of strong solvent evaporation and its consequences for the following drying steps. A criterion predicting whether or not Bénard–Marangoni instability effectively occurs will be discussed. Finally, we report a non-classical delamination mode generating fragments with convex surfaces, whereas buckle-driven delamination usually results in concave shapes.

Received 10th December 2018,
Accepted 25th January 2019

DOI: 10.1039/c8sm02494d

rsc.li/soft-matter-journal

1 Introduction

Film formation by drying of colloidal dispersions is a widely used process in many industrial applications,^{1,2} and in particular coating engineering. A thin layer of a colloidal dispersion is poured onto the surface of a material and a dry solid film is obtained through the evaporation of the volatile liquid, modifying the material surface properties. The success of the coating process depends on the properties of the final deposited film, because it determines essential functions of the material such as optical properties (reflectance or absorption), chemical resistance (against corrosion or dissolution), strength or other physical properties appropriate for a particular application. Generally, applications require homogeneous, smooth surfaces. However, the control (and the understanding) of the drying of colloidal dispersions is highly challenging because of the complexity of the process which involves several intricate physico-chemical phenomena, such as solvent evaporation, transport of matter and heat (diffusion, convection), a sol–gel transition, mechanical stress development in the consolidated film, *etc.* The final quality of the coating can be strongly affected by instabilities that develop during the evaporation. It has been reported in many studies that the stresses, when too great, are released through (often detrimental) mechanical instabilities such as creases,³ shear bands,^{4,5}

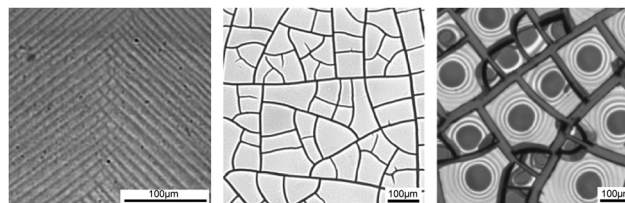


Fig. 1 Images of various morphologies of films resulting from the drying of an aqueous colloidal dispersion. The development of mechanical stress can lead for instance to shear bands (left), channeling cracks (center) or delamination (right). The left image is reproduced from *Phys. Rev. Lett.*, 2015, **115**, 088302.⁵ Copyright 2015 American Physical Society.

cracks^{6–10} and film delamination^{11–13} offering a surprising variety of patterns, as partially illustrated in Fig. 1.

Most of the fundamental studies concerning the drying of colloidal dispersions consider aqueous dispersions. However, in addition to its fundamental interest, for industrial and technological perspectives the use of highly volatile solvents could be relevant to accelerate the drying rates, and hence to decrease the production times. As this question is still open, we here investigate the influence of the solvent volatility on the drying of colloidal films by considering the drying of millimeter-thick layers of a colloidal dispersion made of isopropanol, a highly volatile solvent. The observed behavior is compared to the one of a classical water-based dispersion used as a reference. We highlight that the phase change kinetics strongly influences the formation of the film by affecting the underlying hydrodynamics. The drastic consequences for the following drying

^a TIPS lab – Fluid Physics, Université libre de Bruxelles, Brussels, Belgium.
E-mail: bsobac@ulb.ac.be

^b FAST lab UMR 7608 CNRS, Orsay, France

steps, from the film consolidation to the final morphology of the films, are reported. Finally, a criterion for avoiding the development of Bénard–Marangoni instability and the heterogeneous consolidation of colloidal films is discussed. The present study complements the previous work of de Gennes,¹⁴ Bassou and Rharbi,¹⁵ and Doumenc *et al.*^{16–18} concerning the occurrence of convective instabilities during the drying of polymer suspension systems. However, it is a thermal (and not a solutal) instability which is at play in the present case.

2 Materials and methods

The experiments consist of drying films of colloidal suspensions in ambient air at rest ($T = 20\text{--}25\text{ }^\circ\text{C}$, $P = 1\text{ atm}$ and $H = 55\%$). A schematic of the experimental set-up is provided in Fig. 2(a). Two colloidal suspensions of different volatilities are used in this study. Both suspensions contain silica particles (SiO_2) of diameter $2R_p = 25\text{ nm}$ with an initial mass fraction $\rho_{w_0} = 10\text{--}15\%$. The main difference between the suspensions lies in the solvent. One suspension is composed of water (Ludox TM-50 from the company Sigma-Aldrich) whereas the other one is based on

isopropanol (SiO_2 nanoparticle dispersion in 2-propanol from the company US Research Nanomaterials, Inc.), a highly volatile liquid. The Ludox TM-50 is provided with an initial mass fraction of 50% and is consequently diluted with pure distilled water to reach the same initial mass fraction as the other suspension.

An experiment starts by pouring a certain amount of a colloidal suspension into a circular container to form a layer of desired thickness. Millimeter-thick layers are mainly considered in this study. During the drying process, the mass, m , is measured using a precision scale (Sartorius CPA10035). The initial film thickness h_0 is deduced from the initial weight considering $h_0 = (m_0 - m_{\text{men}})/\rho_{s_0}S$, where m_{men} is the mass of the liquid meniscus against the internal cylinder wall, $\rho_{s_0} = \phi_0\rho_p + (1 - \phi_0)\rho_\ell$ is the initial colloidal suspension density, S is the container surface area and ϕ_0 is the initial particle volume fraction. ρ_p and ρ_ℓ are the densities of the particles and the solvent, respectively. The particle mass and volume fractions are related according to $\phi_w = (\rho_p/\rho_s)\phi$. More precisely, m_{men} is theoretically estimated assuming that the meniscus is in its hydrostatic equilibrium state. The evaporation rate, dm/dt , is extracted from the mass measurements. Simultaneously, the morphological evolution of the film is recorded either with an optical camera (Nikon D3100) or an infrared camera (Thermosensorik, InSB 640 SM) looking at the sample from above. The IR camera enables visualizing potential thermal fluctuations that could show up as a result of a Bénard-type instability, therefore also revealing the presence of convective flows (see *e.g.* ref. 19).

After the complete drying of the layer, the resulting dried film is analyzed using a 3D confocal microscope (Keyence VK-X200 series) in order to characterize the shape of the final solid deposit. The final film thickness h_f is estimated from the initial mass of the film according to $h_f = \rho_{w_0}(m_0 - m_{\text{men}})/(\rho_p\phi_{\text{cp}}S)$ where $\phi_{\text{cp}} = 0.64$ is the random close packing volume fraction for spherical particles.

Various containers have been used in order to detect any potential influence of the material and of the size of the substrate on our results: a glass petri dish (height $H = 1.3\text{ cm}$ and inner diameter $d = 3.4\text{ cm}$), a plexiglass dish ($H = 1.3\text{ cm}$ and $d = 8.5\text{ cm}$) and a PVC cylinder glued to a black aluminium plate ($H = 1\text{ cm}$ and $d = 3.4\text{ cm}$). The latter is mainly used combined with the IR camera because of its emissivity $\varepsilon = 1$ that allows better IR visualization.

The height of the container walls can be easily tuned by extending the borders with a PVC cylinder (of the same diameter) and wrapping them with scotch tape in order to avoid any vapor leaks. Changing the vapor transfer distance $H-h$ in the gas allows us to vary the evaporation rate (see eqn (1)) and to investigate the influence of the drying kinetics on the presence of convective flows. Using additional cylinders of various heights permits us to set H to 1 cm, 2.4 cm, 3 cm, 4 cm and 5.4 cm.

3 Experimental results

3.1 Drying of an aqueous colloidal suspension

The drying kinetics of an aqueous colloidal dispersion is shown in Fig. 3(a) where the time variations of the mass, m , and of the drying rate, dm/dt , are reported. One classically observes that

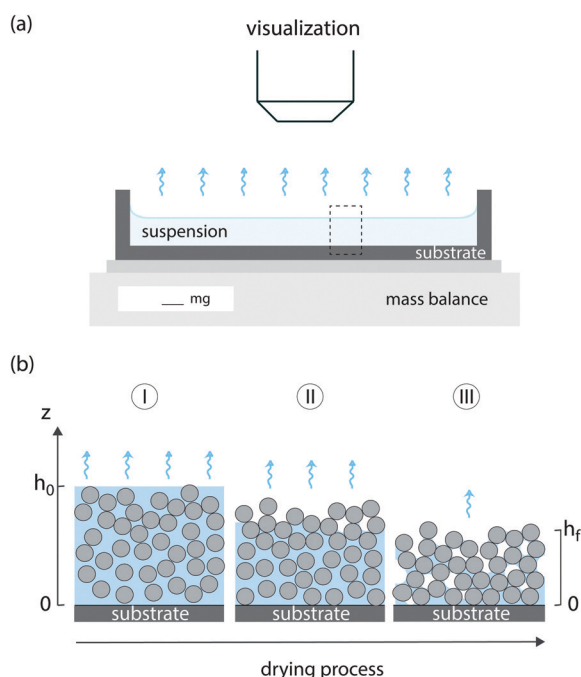


Fig. 2 (a) Experimental setup (side view). A colloidal suspension is deposited in a circular container and allowed to dry. During evaporation, the colloidal film is weighed with a mass balance and visualized by either an optical or an infrared camera. The solvent evaporation from the free surface induces consolidation of the film. The region shown in the dashed rectangle is sketched in (b). The series of sketches illustrates the structuration of the layer during the drying. The first regime, I, the constant rate period (CRP), is characterized by the presence of a continuous liquid network through the layer. The dispersion evaporates as a pure solvent while the particle volume fraction increases over time. When a close packed array of particles is formed, further evaporation leads to a second regime, II, the first falling rate period (FRP1), where the liquid recedes inside the pores of the solid network. Finally, the remaining liquid patches still trapped in the solid matrix continue to evaporate during regime III, the second falling rate period (FRP2).

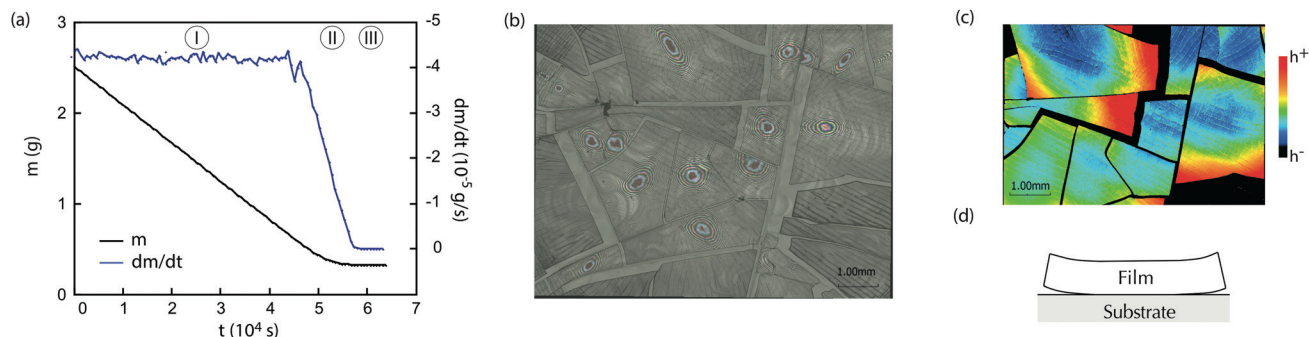


Fig. 3 Drying of a layer of an aqueous dispersion of silica particles (Ludox TM). (a) Variations of the mass, m , and the evaporation rate, dm/dt , over time. Three periods are emphasized: (I) the constant rate period where the dispersion evaporates similarly to a pure solvent, (II) the first falling rate period corresponding to a liquid–solid transition and (III) the second falling rate period where the remaining liquid bridges/patches finish evaporating to complete the drying. (b) Image of the resulting solid film. The final pattern reveals the presence of cracks. The solid fragments delaminated as evidenced by the interference fringes in (b) and confirmed by the 3D scan image in (c). The edges of the solid fragments are lifted, generating concave surfaces as illustrated by scheme (d) in a side view. Here, the substrate is in glass, $h_0 = 2.36$ mm and $h_f = 195$ μ m.

the drying process is separated into three stages, with which different physical processes are usually associated.^{8,20,21}

Initially, a constant rate period (CRP) takes place. In this regime, the evaporation rate is constant, close to the evaporation rate of a pure solvent. Indeed, this regime is associated with the presence of a continuous liquid network through the layer (see I in Fig. 2(b)). Hence, the evaporation is mainly controlled by the vapor diffusion into air and depends on the external conditions of relative humidity and temperature of the surroundings. While drying, the film consolidates. Indeed, when the solvent evaporates at the free surface, the film thickness decreases and the volume fraction of particles increases in time.^{2,3,22–24} Thus, the particles, mainly transported downwards by the receding motion of the free surface and by their own diffusion, progressively build a solid network inside a uniform flat film saturated with solvent. The consolidation mechanisms are further discussed in Section 4.2.

When the solid network reaches a close packed array state and shrinkage stops, further evaporation drives a progressive liquid recession into the porous medium formed by particles (see II in Fig. 2(b)). Then, a non-linear drying rate period, namely the first falling rate period (FRP1), follows when the drying rate decreases with time because of the increasing diffusional resistance to evaporation from the liquid–air interface to outside the porous structure.

Finally, at some point the liquid phase breaks up into separate fractions (see III in Fig. 2(b)) and the drying process enters into a second falling rate period (FRP2) completing the drying. The associated drying rate is much slower than those of the two first regimes.

During the drying, capillary forces that are generated by the development of liquid–air menisci at the free surface apply a compressive stress on this network, which usually relaxes through the propagation of cracks within the solid layer. As a result, cracks invade the plane of the layer, thus dividing this plane into polygonal adjacent cells, *i.e.* fragments, adhering on the substrate (see Fig. 3(b)). The cracks usually occur for aqueous dispersions at the end of the CRP.⁸ The fragment size has extensively been described as a function of the thickness in various systems and increases with the thickness.¹⁰ Since the fragments themselves are even more compressed on the drying face, differential shrinkage in

the film takes place. A delamination process generally follows when the stored elastic strain energy overcomes the adhesion energy of the gel attached to the substrate.¹¹ This results in out-of-plane deformations which lift the edges of the cell and generate concave surfaces, as sketched in Fig. 3(c).

This description corresponds to the usual behaviour encountered during the formation of films from waterborne colloidal dispersions, in a wide range of solid layer thicknesses. Below a critical thickness of about 1 μ m, layers appear to be free of cracks.¹⁰ The delamination process occurs for layer thicknesses above a critical thickness²⁵ of about 8 μ m for layers made of Ludox TM-50 particles.

3.2 Drying of an isopropanol-based colloidal suspension

The drying kinetics of the isopropanol-based dispersion (see Fig. 4(a)) is similar to the one of the aqueous suspensions. A faster evaporation period with a constant rate is followed first by a drastic decrease of the evaporation rate in a second phase, and finally by the second falling rate period completing the drying in agreement with the usual picture provided in the previous section. However, two main differences can be observed. First, the magnitude of the evaporation rate is higher by about four times due to the higher volatility of the isopropanol. Second, the dimensionless evolution of the evaporation rates (using the characteristic drying time defined below eqn (2) as the timescale) shows the CRP ends faster by about 20%.

As illustrated in Fig. 5(a–g), the succession of the main mechanisms usually reported during the drying of a colloidal suspension still occurs here, *i.e.* evaporation of the solvent, consolidation of the layer, crack formation and delamination. However, during the beginning of the constant rate period, the visualization of the sample with an IR camera highlights in this case the existence of thermal fluctuations with a hexagonal-like pattern. Such an observation is typical of the development of thermal Bénard–Marangoni instability (*cf.* Section 4.3). Interestingly, in such a situation, a preferential accumulation of particles and then consolidation of the layer is observed at the liquid–air interface at the border of the hexagons. It most likely results from the particle transportation by the convective flow to the

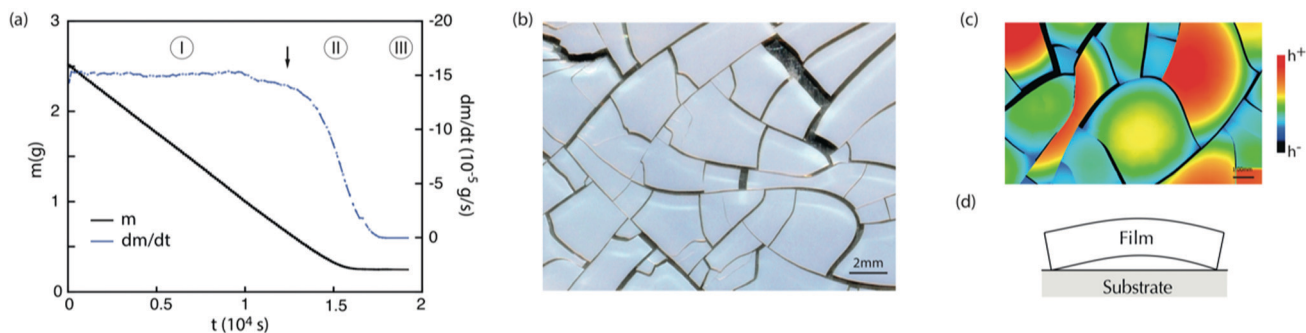


Fig. 4 Drying of a layer of an isopropanol dispersion of silica particles. (a) Mass and evaporation rate evolutions. Three periods are observed as for the drying of an aqueous colloidal dispersion (see Fig. 3(a)). The arrow indicates the time of crack formation for the film. (b) Observation of the final solid film evidences the presence of cracks. (c) The 3D scan reveals a different shape of the solid fragments in this case. Convex surfaces are observed as illustrated by the scheme in panel (d). Here, the substrate is made of glass, $h_0 = 2.72$ mm and $h_f = 195$ μm .

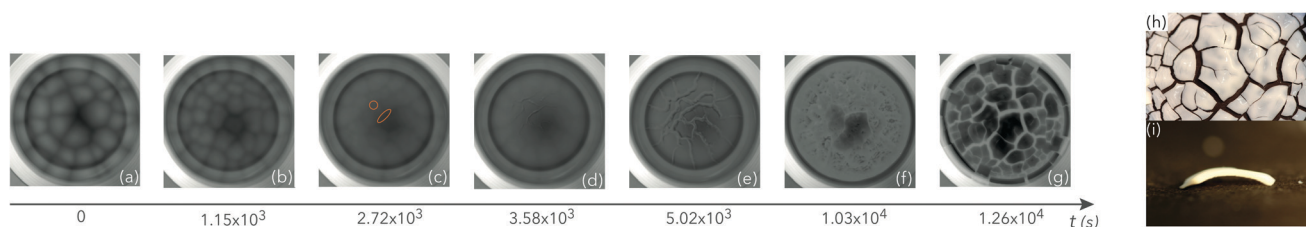


Fig. 5 (a–g) Infrared snapshots of the drying of a layer of an isopropanol dispersion of silica particles with an initial thickness $h_0 = 1.34$ mm on an aluminum substrate. (a and b) A hexagonal cellular pattern resulting from the thermal Bénard–Marangoni instability develops and evolves over time. (c and d) The particles preferentially accumulate at the border of the convective cells and the layer consolidates with a corrugated surface (e) that will crack (f) and delaminate, resulting in the final pattern given in (g). (h and i) Direct visualization of the final solid film (top view) and of a solid fragment revealing a convex geometry (side view), respectively. The inner diameter of the container is 3.4 cm.

stagnation points. Further evaporation leads to the complete consolidation of the layer leading to a non-homogeneous film presenting a corrugated surface. Whereas initially the preferential consolidation can form well-ordered hexagons at the film surface, the shape of the consolidated interface evolves during the drying of the layer leading at the end to an interface presenting what seems to be arbitrary corrugations.

Surprisingly, after the crack invasion of the layer plane, an unusual delamination occurs generating fragments with convex surfaces, as shown in Fig. 4(c) and 5(i). The curvature of the dried fragments appears to be reversed compared to what is usually observed.

Fig. 6 provides a spatio-temporal picture revealing the morphological evolution of the drying layer. It shows the whole process from the consolidation with a corrugated free surface on the left side to the final pattern composed of delaminated convex solid fragments on the right side.

Note that the present observations concerning the drying of the millimeter-thick isopropanol-based colloidal dispersion were reproducible on the various substrates investigated: glass, smooth plexiglass and rough aluminium.

4 Discussion

4.1 Film evaporation

Consider a liquid layer of thickness h with a flat interface evaporating into a vapor–air gas mixture taken as ideal. Assuming

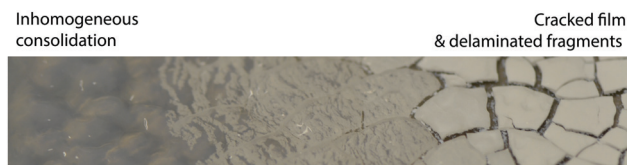


Fig. 6 Image of a layer of a colloidal suspension of SiO_2 particles in isopropanol drying on a tilted plexiglass substrate. This tilt allows one to visualize at the same time the drying of a film of variable thickness, with a thickness that is thicker on the left side and thinner on the right side. The drying time depends on the thickness; the image gives an impression of observing the morphological evolution of the layer from a consolidation step with corrugated surface on the left side to the final pattern composed of delaminated convex solid fragments on the right side, as if the time was running from left to right.

the total pressure of the gas phase p_g to be constant and uniform, and that the evaporation is limited by diffusion in the air, the layer evaporates at a rate (see, *e.g.* ref. 19 and 26):

$$\frac{dm}{dt} = - \frac{D_{va} M_v S}{RT_i} \left. \frac{\partial_2 p_v}{1 - X_i} \right|_{z=h(t)} \quad (1)$$

where D_{va} is the vapor–air diffusion coefficient, M_v is the molar mass of the vapor, p_v is the partial pressure of the vapor in the gas phase, $X = p_v/p_g$ its mole fraction, R is the ideal gas constant, T is the temperature and S is the liquid–gas interfacial area that can be considered equal to the cylinder cross section, as a

first approximation. The subscript i denotes a quantity evaluated at the layer free interface.

During the first phase of the drying of a colloidal suspension (CRP), the evaporation kinetics is identical to that of a pure liquid (the presence of particles is assumed not to have any effect on the solvent partial pressure, and they are supposed to be completely wetted by the liquid). Indeed, the evaporation rate remains constant (as corroborated by Fig. 3(a) and 4(a)) and the film thickness decreases linearly over time according to

$$h(t) = h_0 + \frac{1}{\rho_\ell S} \frac{dm}{dt} t. \quad (2)$$

From eqn (2), a characteristic drying time $\tau_{ev} = h_0/V_E$ can be derived where $V_E = -\frac{1}{\rho_\ell S} \frac{dm}{dt}$ is the drying velocity in m s^{-1} .

4.2 Consolidation of a drying colloidal film in the absence of convective instabilities

The solvent evaporation at the free surface leads to the consolidation of the drying layer. Indeed, the particle volume fraction, ϕ , increases as the film thickness decreases, the total amount of particles being unchanged. If no bulk flow occurs, the time and spatial variations of the particle volume fraction are usually described by a one-dimensional diffusion equation for $\phi(z,t)$:^{3,22–24,27}

$$\frac{\partial \phi}{\partial t} = \frac{\partial}{\partial z} \left(D(\phi) \frac{\partial \phi}{\partial z} \right) \quad (3)$$

where $D(\phi)$ is the collective diffusion coefficient that in general depends on the particle volume fraction.²² Boundary conditions on eqn (3) express that the flux of particles at the film bottom vanishes, while at the liquid–air interface it matches the recession due to evaporation (*i.e.* the particles do not cross the interface):

$$\frac{\partial \phi}{\partial z} = 0 \quad \text{at } z = 0 \quad (4)$$

$$D(\phi) \frac{\partial \phi}{\partial z} = \phi_i V_E \quad \text{at } z = h(t). \quad (5)$$

$\phi_i(t) = \phi(0,t)$ is the particle volume fraction at the receding interface. Eqn (3) under the boundary conditions (4) and (5) and the initial condition $\phi(z,0) = \phi_0$ can be solved numerically. The solution provides the evolution of the particle volume fraction profile across the drying layer.

The distribution of particles is known to be controlled by a Péclet number,²² $Pe = h_0 V_E / D_0$, quantifying the relative importance of interface recession and diffusion on particle transport. $D_0 = k_B T / 6\pi\mu_\ell R_p$ is the Stokes–Einstein diffusion coefficient, where k_B is Boltzmann's constant, μ_ℓ is the solvent viscosity and R_p is the particle radius. Hence for $Pe \ll 1$, diffusion is strong and uniform particle profiles are expected, while for $Pe \gg 1$, large gradients in volume fraction are expected. An estimation for our experiments leads to $Pe > 1$. As a consequence, a region of close packed particles builds up at the top surface first and then progresses into the film. As time goes on, the entire flat film tends towards close packing, as sketched in Fig. 7(a).

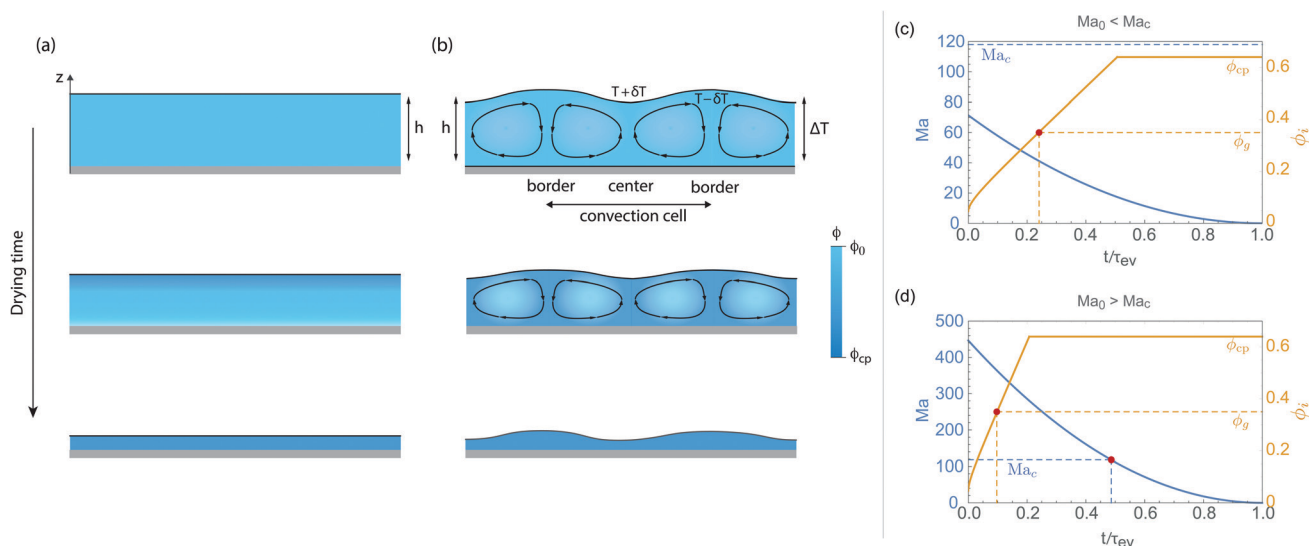


Fig. 7 (a and b) Schematic evolutions of the layer thickness and particle volume fraction during the drying of a colloidal layer (a) without and (b) with the presence of convective cells. Whereas in the first case, the consolidation scenario corresponds to Section 4.2 and leads to the formation of a homogeneous dry film, in the second case, Bénard–Marangoni instability affects the concentration field leading to the formation of an inhomogeneous dry film. (c and d) Evolutions of the Marangoni number and of the interface particle volume fraction during the drying of a layer of an isopropanol dispersion of silica particles with two initial thicknesses: (c) $h_0 = 400 \mu\text{m}$ and (d) $h_0 = 1 \text{ mm}$. In panel (c), $Ma_0 < Ma_c$, no Bénard–Marangoni instability develops in the drying film. The suspension at the interface undergoes a glass transition at about $0.22t/\tau_{ev}$ and reaches a close packed structure at about $0.5t/\tau_{ev}$. This scenario is sketched in panel (a). In panel (d), $Ma_0 > Ma_c$, Bénard–Marangoni instability develops in the drying film. One observes that the disappearance of the instability is reached at a time $\tau_{BM} \approx 0.5\tau_{ev}$ well after the gelation time of the interface $\tau_g \approx 0.1\tau_{ev}$. This scenario leads to the consolidation of an inhomogeneous film, as sketched in panel (b). Note that for isopropanol, $V_E \approx 1.86 \times 10^{-7} \text{ m s}^{-1}$ and $h_c = 520 \mu\text{m}$ in the cases illustrated in panels (c and d).

Assuming $D(\phi) = D_0$ when $\phi < \phi_{cp}$ and since $V_E = \text{cste}$ in the CRP, one can obtain an analytical expression of the solution. In particular, we have an expression for $\phi_i(t)$ as²³

$$\phi_i(t) = \phi_0 - 2\delta\phi_0 \int_0^t \left[\frac{\exp(-\delta^2 t')}{\sqrt{\pi t'}} - \delta \operatorname{erfc}(\delta\sqrt{t'}) \right] dt' \quad (6)$$

with $\delta = V_E / (2\sqrt{D_0})$. This equation expresses the evolution of the particle volume fraction at the interface from the initial volume fraction ϕ_0 to the close packing ϕ_{cp} . This solution is plotted in Fig. 7(c and d) for $V_E \approx 2 \times 10^{-7} \text{ m s}^{-1}$ and two initial layer thicknesses.

During evaporation, colloidal dispersions exhibit different structural properties, from the fluid-like phase to the wet aggregated solid, crossing a soft colloidal glass phase where the medium exhibits a finite shear modulus. Experiments performed on aqueous colloidal dispersions have clearly shown the existence of a liquid to solid-like transition at a concentration well below close packing.^{3,28–30} Typically, the rheology of silica colloidal dispersions varies from viscous to elasto-visco-plastic to brittle when their solvent content decreases.³⁰ The sol-gel transition appears to occur at a critical volume fraction^{3,29,30} $\phi_g = 0.3\text{--}0.35$, which is also indicated on the curves presented in Fig. 7(c and d).

4.3 Bénard–Marangoni instability induced by evaporation

Due to the latent heat needed for evaporation, a layer of volatile solvent deposited on a substrate is subject to a temperature variation between the substrate and the free surface. Considering conductive heat transfer in the layer (and neglecting the heat coming from the gas phase, since $\lambda_g \ll \lambda_\ell$ in general), the evaporation-induced temperature difference across the thickness layer can be estimated by

$$\Delta T = -\frac{\dot{m}\mathcal{L}h}{\lambda_\ell S} \quad (7)$$

where \mathcal{L} is the latent heat of vaporization, while λ_ℓ and λ_g are the liquid and gas thermal conductivities, respectively.

It is well known that due to this temperature gradient and the variation of the surface tension with temperature, the evaporation can induce the development of Bénard–Marangoni instabilities in a pure liquid film.^{19,26,31,32} When the Marangoni number $\text{Ma} = -\gamma_T \Delta T h / \mu_\ell \kappa_\ell$ (where γ_T is the surface tension variation with the temperature and κ_ℓ is its liquid thermal diffusivity) is above a critical value Ma_c , such instabilities develop and the layer self-structures into an hexagonal convective pattern, as sketched in Fig. 7(b). In this situation, the coupling between thermal fluctuations and resulting surface-tension-induced flows is sufficiently strong to overcome thermal and viscous dissipation, resulting in more or less ordered cellular convective patterns.³³ In each “cell”, liquid is rising at the warmer center, flows along the interface from hot to cold, sinks downwards at the cooler cell periphery, and closes the loop by flowing towards the center. Note that below Ma_c , such instabilities do not appear and the layer remains in a purely conductive regime.

The modeling of evaporation-driven Bénard–Marangoni convection in a liquid layer of thickness h much smaller than

the gas phase thickness H , leads to the expression of the neutral stability threshold¹⁹

$$\text{Ma}_k = \frac{16k(k \cosh[k] + \alpha k \sinh[k])(2k - \sinh[2k])}{4k^3 \cosh[k] + 3 \sinh[k] - \sinh[3k]} \quad (8)$$

where k is the dimensionless wavenumber and

$$\alpha = \frac{\lambda_g}{\lambda_\ell} + \frac{\mathcal{L}D_{va}M_v p'_{\text{sat}}(T_i)}{\lambda_\ell RT_i(1 - X_i)} \quad (9)$$

is a positive dimensionless number that turns out to be an effective gas-to-liquid ratio of thermal conductivities, accounting for phase-change-induced heat spreading (due to latent heat transport by vapor diffusion) through its second term. Note that eqn (8) is formally identical to the result obtained by Pearson,³¹ up to a redefinition of the Biot number as $\text{Bi} = \alpha k$, *i.e.* wavenumber-dependent.^{19,26} With this difference in mind, the critical Marangoni number $\text{Ma}_c(\alpha)$ and the critical wave number $k_c(\alpha)$ are found by minimizing Ma_k with respect to k . It is interesting to note that α only depends on the liquid–gas pair, and increases with the volatility. For isopropanol evaporating in air at ambient conditions, $\text{Ma}_c \approx 120$, whereas for water, $\text{Ma}_c \approx 90$.

Combining the definition of the Marangoni number given above with eqn (7), a critical layer thickness can be derived

$$h_c = \left(-\frac{\lambda_\ell \mu_\ell \kappa_\ell S}{\gamma_T \dot{m} \mathcal{L}} \text{Ma}_c(\alpha) \right)^{1/2}. \quad (10)$$

Indeed, when the initial film thickness $h_0 > h_c$ (equiv. to an initial Marangoni number $\text{Ma}_0 > \text{Ma}_c$), a Bénard–Marangoni instability develops and hexagonal cells show up in the evaporating film. During evaporation, the characteristic size of a convective cell, which is typically of the order of the film thickness, decreases over time. At some moment, when $h < h_c$, convection cells can not persist, leading to the conductive regime. Chauvet *et al.*¹⁹ experimentally validated this criterion for pure liquids of various volatilities, recovering in particular the classical value $\text{Ma}_c \approx 80$ in the weakly-volatile case $\alpha \ll 1$.

Note also that the characteristic time after which Bénard–Marangoni convection stops can be estimated as

$$\tau_{\text{BM}} = (h_0 - h_c)/V_E. \quad (11)$$

4.4 Consolidation of a drying colloidal film in the presence of convective instabilities

When Bénard–Marangoni instability occurs during the drying of a colloidal dispersion ($\text{Ma}_0 > \text{Ma}_c$), as reported in this paper for millimeter-thick isopropanol-based dispersions, then convective transport is superposed onto the diffusion flux, as sketched in Fig. 7(b). Since the diffusion of particles is slow, the particles are mainly transported by flows, including the receding motion of the interface. The combination of these mechanisms leads to an inhomogeneous distribution of particles in the layer and a corrugation of the free surface (see Fig. 7(b)). The particles preferentially accumulate at the stagnation points of the free surface, located at the edges of the cells (where the temperature is smaller). Some trace of the concentration field inhomogeneity

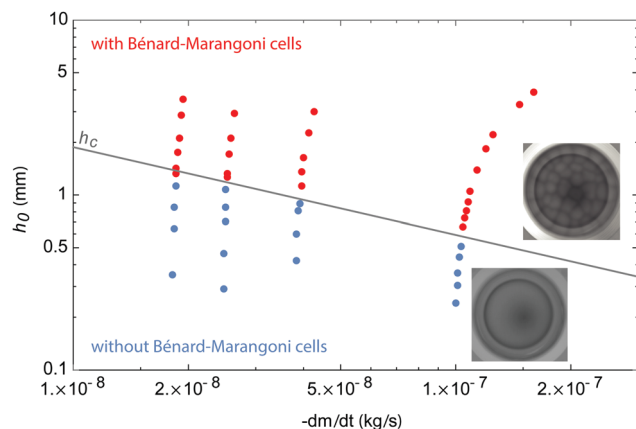


Fig. 8 Existence phase diagram of Bénard–Marangoni instability during the drying of a colloidal suspension of silica particles dispersed in isopropanol as a function of the initial thickness and the evaporation rate. The bullets correspond to experimental data while the line represents the theoretical onset of the Bénard–Marangoni instability predicted by eqn (10). The IR images attest to the presence (top) or the absence (bottom) of convective flows.

is likely to be “frozen” in the drying film when consolidation occurs before the convective cells cease, as in Fig. 7(d). The evolution of the Marangoni number and of the particle volume fraction at the film free surface is plotted during the drying of a millimeter-thick isopropanol-based dispersion evaporating into air under ambient conditions. In such a situation, one observes that the surface concentration reaches the gelation concentration at a time significantly shorter than the time needed for the convective motions to stop.[†] One can therefore expect the drying to lead to the consolidation of a distorted free surface followed after further evaporation by the consolidation of an inhomogeneous film presenting surface corrugations, as evidenced in Fig. 9(a–c). The consolidation of a film with a corrugated free surface could occur even though the convection has ceased, if the diffusion time of particles is longer than the time between the convective cells’ disappearance and the film consolidation. Ultimately, the solid film is expected to be thicker and convex where the concentration of particles was highest, and thinner/concave at locations where it was lowest.

To check the validity of the criteria presented in eqn (10) for colloidal suspensions, experiments were conducted with isopropanol-based dispersion layers of various initial thicknesses and for several evaporation rates (see the Method in Section 2). The resulting existence phase diagram of thermal Bénard–Marangoni instability during the drying of our colloidal suspension as a function of the two parameters is shown in Fig. 8. The theoretical prediction of the instability onset (eqn (10)) is also plotted and is found to be in good agreement with the experimental results. When experiments occur with layers of initial

[†] Note that the evolution of the particle volume fraction at the free surface is plotted according to eqn (6), which only considers diffusive transport in the film. Consequently, the time for the particle volume fraction at the free surface to reach the gelation volume fraction could well be even shorter, with convection cells enhancing the transport, and the accumulation of particles at the stagnation points.

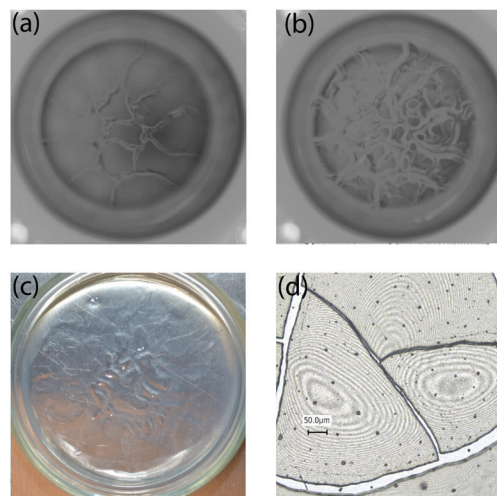


Fig. 9 (a and b) Infrared and (c) direct visualization highlighting (a) the accumulation of particles at the borders of the convective cells and (b and c) the consolidation of a film with corrugations at the top surface during the drying of a colloidal suspension of the isopropanol-based dispersion on various substrates with $h_0 > h_c$ (aluminum substrate (a and b) and glass substrate (c)). (d) Image of the resulting solid film obtained after the drying of the isopropanol-based dispersion with $h_0 < h_c$. The interference fringes reveal that in such a situation the solid fragments classically delaminate with a concave shape, the pattern of interference fringes being similar to the one observed for aqueous dispersions (*cf.* Fig. 3(b)).

thicknesses h_0 below the critical thickness h_c (equiv. $Ma_0 < Ma_c$), no thermal convective patterns were indeed discernable with the infrared visualisation, confirming that the drying is occurring in a conductive regime as revealed by the IR image presented at the bottom of Fig. 8 that exhibits an homogeneous thermal field. The present experiments suggest that the rate of solvent evaporation is an important parameter for the homogeneity of the resulting film. It is indeed confirmed by eqn (10). High values of $|m|$ lead to low values of h_c . The Bénard–Marangoni instability (which occurs for $h > h_c$) is favoured by an increase of the evaporation rate.

However note that the influence of the solvent evaporation rate does not fully explain the absence of Bénard–Marangoni instability for aqueous dispersions. Indeed, whereas Marangoni flows induced by evaporation have been observed in many pure liquids, their existence for water is dubious.^{34–37} Despite conditions where the hydrodynamic theory indicated that it should be present ($Ma_0 > Ma_c$), the observation of Marangoni convection has been non-reproducible and/or transient. This is generally attributed to contamination on the surface of the water.^{34,35,38,39} It was shown theoretically that the presence of even trace amounts of surface contamination can stabilize a water layer by mitigating or suppressing the evaporation-induced thermocapillary flows.^{38,39} In practice, a tiny presence of contamination at water surfaces appears to be almost unavoidable, water being easily contaminated.^{36,37} This could well explain why experimental studies dealing with millimetric thick layers of aqueous dispersions in general did not report surface-tension-driven convective instabilities. To the best of our knowledge, only Boulogne *et al.*⁴⁰ experimentally observed convective cells during the drying of aqueous suspensions.

However, in their experiments, convection ceases before the film consolidation leaving time for the film to recover its homogeneity.

As mentioned by de Gennes,¹⁴ the instability requires films to be initially dilute and of low viscosity. Eqn (10) shows indeed that the suspension viscosity is another important parameter, of which a high value is unfavourable to the development of Bénard–Marangoni instability. Since the dispersion viscosity drastically increases when ϕ gets close to ϕ_g ,³⁰ a concentrated colloidal film would imply a very large value of h_c . Moreover, if the drying occurs with ϕ_0 close to ϕ_g , the layer could in principle even consolidate before the establishment of the convective instability.

4.5 Crack formation and curled fragments

The formation of a structure induced by the drying requires the development of a shear modulus of the particle arrangement. As a consequence, the structure can withstand drying stresses that progressively build in the solid film. When a threshold value is reached, the drying stress is released into the solid film by the formation of successive modes of cracking.¹⁰ Classically, first cracks invade the plane of the film resulting in a connected network of cracks.⁴¹ The size of the resulting solid fragments as a function of the solid film thickness for both the water-based and isopropanol-based dispersions is reported in Fig. 10. The measurements of the average solid fragment size appear to be well described by the $a_s \propto h_f^{2/3}$ scaling law reported in ref. 42. The standard deviation around the average value of the solid fragment sizes obtained by statistical analysis of the final crack patterns is also provided in Fig. 10. Interestingly, one observes that the standard deviations for the water-based dispersion are

relatively small and almost constant as a function of the film thickness. It is however not the case for the isopropanol-based dispersion where the standard deviations reveal an important contrast between the experiments that occurred below or above the Bénard–Marangoni onset of instability. In particular, the standard deviations are higher for experiments for which convective flows developed during the drying. It highlights a higher heterogeneity in the fragment size distribution in these situations likely due to the presence of the corrugations induced by the Bénard–Marangoni instability. Below the onset of instability, the analysis of the solid fragment shapes interestingly reveals that delamination results in the usual concave solid fragment shapes, as seen in Fig. 9(d). This observation supports the role of the corrugations, and hence of the convective flow, in the occurrence of convex solid fragments for isopropanol-based dispersion layers with $h_0 > h_c$.

The prefactor of the scaling law⁴² allows us to determine the elastic modulus of the solid film at the time cracks form. Rather than considering the values of the elastic moduli that are not precisely determined due to the difficulty of quantifying the drying stress, in particular the capillary pressure, we only consider the ratio between the elastic moduli of the water-based film, E_w , and isopropanol-based film, E_{iso} : $E_w/E_{iso} = 0.21 \pm 0.05$. This ratio shows a stiffer coating for the isopropanol-based dispersion than for the water-based one.

Once the solid film has cracked, if the fragments are still compressed on the drying face, differential shrinkage takes place on both sides of the film thickness. The differential shrinkage is governed by the variation of liquid pressure in the pore and results from a stress distribution, σ_{ij} , in the thickness of the film, that evolves during the drying process^{11,20,43} (the subscripts i, j refer to the cartesian coordinates in the plane of the film). Hence, the shrinkage of the drying film is quantified by a force, $F(t)$, per unit length, and averaged over the film thickness:

$$F(t) = \int_0^{h_f} \sigma_{x,x}(z, t) dz, \quad (12)$$

according to Fig. 11. Consequently a bending moment, $M(t)$, per unit length, develops as

$$M(t) = \int_0^{h_f} (z - h/2) \sigma_{x,x}(z, t) dz. \quad (13)$$

The maximum stress, σ_m , reached in the solid film is close to the capillary pressure given by the surface tension, $\gamma_{\ell,air}$, of the solvent with the air and the pore size close to the particle size R_p . Thus, $\sigma_m \sim -\gamma_{\ell,air}/R_p$. The bending moment tends to induce an out-of-plane displacement which can lift the edges of the fragments. This process is governed by the competition between the elastic energy stored in the structure, $U_{surface}^{el}$, and the surface energy at the film/substrate interface, $U_{surface}^{surf}$, responsible for the adhesion. The elastic energy reaches a maximum value when the stress in the structure reaches σ_m . In this way the elastic energy, per unit surface area of the film, reads

$$U_{surface}^{el} \sim \sigma_m^2 / (2E) h_f, \quad (14)$$

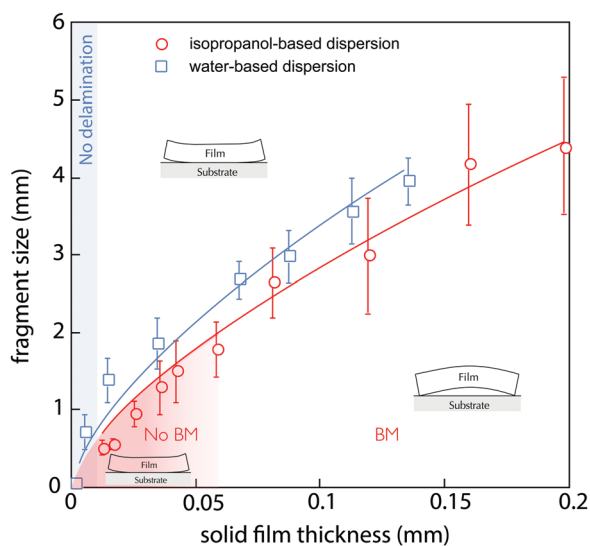


Fig. 10 Fragment size as a function of the final solid film thickness for water-based and isopropanol-based colloidal dispersions. The bars represent the standard deviation around the average value. The data are fitted by the $a_s \propto h_f^{2/3}$ scaling law reported in ref. 42. For thicker films, delamination leads to either concave (water-based) or convex (isopropanol-based) surfaces as evidenced by the 3D scan images in Fig. 3 and 4. For the aqueous dispersion, no delamination occurs below a well-defined thickness (blue region). For the isopropanol-based dispersion, below the Bénard–Marangoni onset (red region), the drying occurs without the development of convective flows and a delamination leading to usual concave surfaces is retrieved, as evidenced by Fig. 9(d).

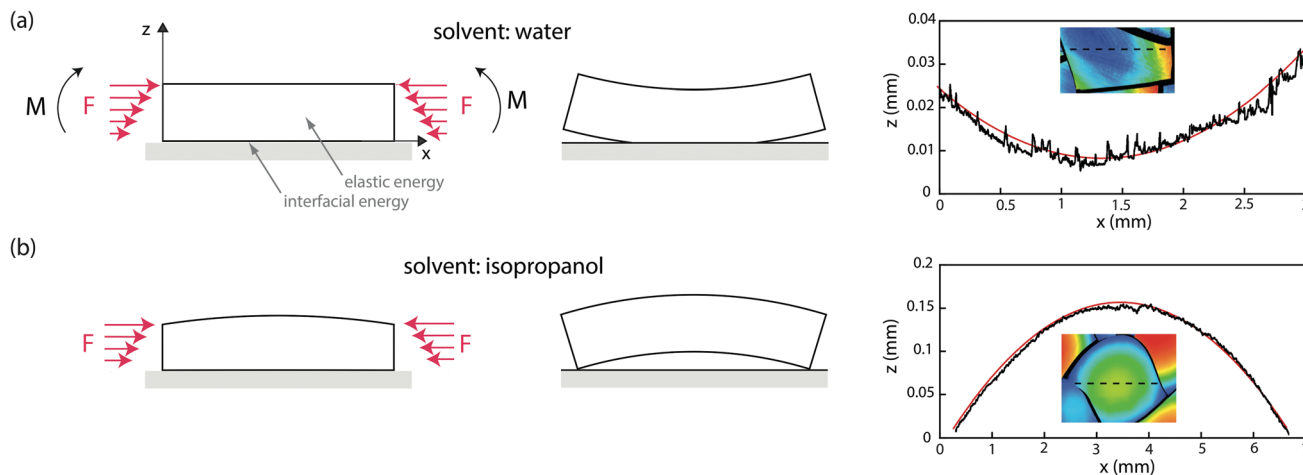


Fig. 11 Buckle-driven delamination of drying films induced by differential stress ($h_f = 195 \mu\text{m}$). (a) Concave final shape in the aqueous-based structure. (b) Convex final shape in the isopropanol-based structure. (Left) Sketches of the scenarios leading to a concave or a convex buckle-driven delamination. As a consequence of differential stress in the film, a force F and a bending moment M develop resulting in a partial de-adhesion of the film. (Right) Experimental measurements of the upper face geometry of solid fragments. The red curves are theoretical shapes of the warped fragments plotted in accordance with eqn (16).

where E is the elastic modulus of the solid film. The surface energy governing the adhesion of the film on the substrate is due to several contributions, among which the van der Waals interactions. However, it has been shown that capillary bridges between nanoparticles and the substrate significantly contribute to the adhesion process of drying colloidal coatings.¹¹ Consequently, the surface energy, per unit surface area of the film, reads

$$U_{\text{surface}}^{\text{surf}} \sim 2\gamma_{\ell, \text{air}}. \quad (15)$$

Thus, the simple criterion $U_{\text{surface}}^{\text{surf}} \geq U_{\text{surface}}^{\text{el}}$ results in the buckle-driven delamination. Since the structure is more compressed on the drying surface, a concave surface is generated as shown in the sketch in Fig. 11(a). The final shape of the warped fragments is related to the maximum bending moment M_m by:⁴⁴

$$\frac{d^2z}{dx^2} = \frac{12M_m}{Eh_f^3} \quad (16)$$

where $M_m \sim \sigma_m h_f^2$. The 3D scan of the fragments allows us to measure the profile of the warped fragments. Fitting the profiles using eqn (16) is then a way to estimate the elastic modulus of the final dried fragments. A similar scenario takes place in the case of isopropanol-based films except that the adhering fragments present an initial convex upper shape induced by the prior hydrodynamical instability as sketched in Fig. 11(b). Since cracks preferentially form at defects, the valleys exhibiting thinner thicknesses represent a favourable location to propagate channeling cracks. Then the formation of the crack network is shortly followed by the delamination process. However, the initial shape is not in favour of the concave deformation naturally induced by the bending moment. The shrinkage induced by the force $F(t)$ (eqn (12)) results in a de-adhesion at the centre of the fragments together with a convex deformation induced by a buckle-driven process. The ratio between the elastic moduli of the water-based film, E_w , and isopropanol-based film

can then be deduced from the fit of the measured profiles using the theoretical prediction of eqn (16): $E_w/E_{\text{iso}} = 0.64 \pm 0.09$. This ratio still shows a stiffer coating for the isopropanol-based dispersion than for the water-based one.

5 Conclusion

In this paper, we report experimental observations on the influence of thermal Bénard–Marangoni instability on the drying of colloidal dispersions.

Considering millimeter-thick films of a silica particles dispersed in isopropanol (a highly volatile solvent), we observe using an infrared camera the existence of a pattern of hexagonal convective cells, from the early stage of the evaporation and as long as the dispersion is dilute. A non-homogeneity of the particle concentration is evidenced by a higher concentration of particles at the cell edges in comparison with the cell center. Together with the solvent removal induced by the evaporation, this hydrodynamical process lead to the consolidation of films with surface corrugations.

The present study clearly reveals the importance of the hydrodynamics during the first phase of fast solvent evaporation to the film morphology. Thus, the development of hydrodynamical instability appears to be detrimental for the homogeneity of the film. A minimal thickness is required to observe this instability. The instability threshold, previously derived from the hydrodynamic theory, is discussed here. This stability criterion also appears to be satisfied for colloidal dispersions and could help to better control the final film homogeneity by selecting an appropriate initial film thickness smaller than the critical value for the occurrence of Bénard–Marangoni instability (here accurately estimated as function of the liquid volatility).

Finally, after the invasion of the solid film by cracks, a non-classical delamination mode occurs generating fragments with convex surfaces, whereas buckle-driven delamination usually

results in concave shapes. A potential mechanical explanation involves a delamination process of a film previously corrugated by coupled hydrodynamics and consolidation. However, other aspects can intervene and we hope further studies will elucidate this intriguing behavior.

Conflicts of interest

There are no conflicts of interest to declare.

Acknowledgements

This work was financially supported by the Fonds de la Recherche Scientifique – F.N.R.S (Postdoctoral Researcher position of BS, Research Director position of PC, DITRASOL contract T.0123.16).

References

- W. B. Russel, *AIChE J.*, 2011, **57**, 1378–1385.
- A. F. Routh, *Rep. Prog. Phys.*, 2013, **76**, 046603.
- F. Boulogne, L. Pauchard, F. Giorgiutti-Dauphiné, R. Botet, R. Schweins, M. Sztucki, J. Li, B. Cabane and L. Goehring, *EPL*, 2014, **105**, 38005.
- B. Yang, J. S. Sharp and M. I. Smith, *ACS Nano*, 2015, **9**, 4077–4084.
- P.-C. Kiatkirakajorn and L. Goehring, *Phys. Rev. Lett.*, 2015, **115**, 088302.
- C. Allain and L. Limat, *Phys. Rev. Lett.*, 1995, **74**, 2981–2984.
- E. R. Dufresne, D. J. Stark, N. A. Greenblatt, J. X. Cheng, J. W. Hutchinson, L. Mahadevan and D. A. Weitz, *Langmuir*, 2006, **22**, 7144–7147.
- L. Pauchard, B. Abou and K. Sekimoto, *Langmuir*, 2009, **25**, 6672–6677.
- L. Goehring, W. J. Clegg and A. F. Routh, *Soft Matter*, 2011, **7**, 7984–7987.
- V. Lazarus and L. Pauchard, *Soft Matter*, 2011, **7**, 2552–2559.
- L. Pauchard, *EPL*, 2006, **74**, 188.
- A. Sarkar and M. S. Tirumkudulu, *Soft Matter*, 2011, **7**, 8816–8822.
- Y. Xu, G. K. German, A. F. Mertz and E. R. Dufresne, *Soft Matter*, 2013, **9**, 3735–3740.
- P. de Gennes, *Eur. Phys. J. E: Soft Matter Biol. Phys.*, 2001, **6**, 421–424.
- N. Bassou and Y. Rharbi, *Langmuir*, 2009, **25**, 624–632.
- G. Toussaint, H. Bodiguel, F. Doumenc, B. Guerrier and C. Allain, *Int. J. Heat Mass Transfer*, 2008, **51**, 4228–4237.
- F. Doumenc, E. Chénier, B. Trouette, T. Boeck, C. Delcarte, B. Guerrier and M. Rossi, *Int. J. Heat Mass Transfer*, 2013, **63**, 336–350.
- S. G. Yiantsios, S. K. Serpetsi, F. Doumenc and B. Guerrier, *Int. J. Heat Mass Transfer*, 2015, **89**, 1083–1094.
- F. Chauvet, S. Dehaeck and P. Colinet, *EPL*, 2012, **99**, 34001.
- C. Brinker and G. Scherer, *Sol–Gel Science: The Physics and Chemistry of Sol–Gel Processing*, Academic Press, New York, 1990.
- P. Coussot, *Eur. Phys. J. B*, 2000, **15**, 557–566.
- A. F. Routh and W. B. Zimmerman, *Chem. Eng. Sci.*, 2004, **59**, 2961–2968.
- T. Okuzono, K. Ozawa and M. Doi, *Phys. Rev. Lett.*, 2006, **97**, 136103.
- L. Goehring, J. Li and P.-C. Kiatkirakajorn, *Philos. Trans. R. Soc., A*, 2017, **375**, 20160161.
- J. Hutchinson and Z. Suo, *Adv. Appl. Mech.*, 1991, **29**, 63–191.
- B. Haut and P. Colinet, *J. Colloid Interface Sci.*, 2005, **285**, 296–305.
- A. F. Routh and W. B. Russel, *AIChE J.*, 2008, **44**, 2088–2098.
- N. Ziane and J.-B. Salmon, *Langmuir*, 2015, **31**, 7943–7952.
- C. Loussert, A. Bouchaudy and J.-B. Salmon, *Phys. Rev. Fluids*, 2016, **1**, 084201.
- E. Di Giuseppe, A. Davaille, E. Mittelstaedt and M. François, *Rheol. Acta*, 2012, **51**, 451–465.
- J. R. A. Pearson, *J. Fluid Mech.*, 1958, **4**, 489–500.
- A. Oron, S. H. Davis and S. G. Bankoff, *Rev. Mod. Phys.*, 1997, **69**, 931–980.
- P. Colinet, J. Legros and M. Velarde, *Nonlinear Dynamics of Surface-Tension-Driven Instabilities*, Wiley-VCH, Berlin, 2011.
- M. J. Block, *Nature*, 1956, **178**, 650.
- J. C. Berg, M. Boudart and A. Acrivos, *J. Fluid Mech.*, 1966, **24**, 721–735.
- G. Barnes and D. Hunter, *J. Colloid Interface Sci.*, 1982, **88**, 437–443.
- H. Cammenga, D. Schreiber, G. Barnes and D. Hunter, *J. Colloid Interface Sci.*, 1984, **98**, 585–586.
- J. Berg and A. Acrivos, *Chem. Eng. Sci.*, 1965, **20**, 737–745.
- H. Hu and R. G. Larson, *Langmuir*, 2005, **21**, 3972–3980.
- F. Boulogne, F. Giorgiutti-Dauphiné and L. Pauchard, *Soft Matter*, 2015, **11**, 102–108.
- S. Bohn, L. Pauchard and Y. Couder, *Phys. Rev. E: Stat., Nonlinear, Soft Matter Phys.*, 2005, **71**, 046214.
- X. Ma, J. Lowensohn and J. C. Burton, *Phys. Rev. E*, 2019, **99**, 012802.
- M. Thouless, A. Evans, M. Ashby and J. Hutchinson, *Acta Metall.*, 1987, **35**, 1333–1341.
- L. D. Landau and E. M. Lifshitz, *Theory of Elasticity (Course of Theoretical Physics)*, Elsevier, 1986, vol. 7.